Delft University of Technology

Delft Center for Systems and Control

Technical report 25-010

An Enhanced Cell-Based Model for Contaminant Dispersion in Marine Environments*

Y. Ma, M. Guo, and B. De Schutter

To cite this work, please refer to the published version:
Y. Ma, M. Guo, and B. De Schutter, "An enhanced cell-based model for contaminant dispersion in marine environments," *Proceedings of the OCEANS 2025 Brest*, Brest, France, 9 pp., June 2025. doi:10.1109/OCEANS58557.2025.11104304

Delft Center for Systems and Control
Delft University of Technology
Mekelweg 2, 2628 CD Delft
The Netherlands
phone: +31-15-278.24.73 (secretary)
URL: `https://www.dcsc.tudelft.nl`

An enhanced cell-based model for contaminant dispersion in marine environments

Ying Ma
Delft Center for Systems and Control
Delft University of Technology
Delft, Netherlands
y.ma-4@tudelft.nl

Meichen Guo
Delft Center for Systems and Control
Delft University of Technology
Delft, Netherlands
m.guo@tudelft.nl

Bart De Schutter
Delft Center for Systems and Control
Delft University of Technology
Delft, Netherlands
b.deschutter@tudelft.nl

Abstract—**In practice, achieving a balance between accuracy, stability, and computational efficiency in modeling contaminant dispersion in marine environments remains challenging due to complex physical dynamics and numerical constraints. To address these challenges, an enhanced cell-based model (CBM) is developed and applied to simulate pollutant transport in the ocean. The CBM discretizes the spatial domain into uniform cells, resulting in a naturally parallelizable structure, and characterizes the transport process by incorporating both water flow-driven convection and diffusion effects. Moreover, two approaches are proposed for estimating the diffusion coefficient, and their performance is compared to a first-order upwind scheme finite-difference method (FDM) solution. Finally, the CBM is comprehensively compared with both the FDM and the finite-element method (FEM) solvers under varying spatial and temporal resolutions. Simulation results show that the CBM is less affected by the Courant–Friedrichs–Lewy (CFL) conditions and demonstrates stable convergence where the FDM fails or requires stricter settings. In addition, the CBM offers a favorable trade-off between accuracy and computational efficiency under coarse configurations. These results indicate that the CBM provides a reliable foundation for dynamic modeling and integration with learning-based frameworks in marine environment simulations.**

Index Terms—**marine pollution, numerical modeling and simulation, dispersion models for marine contaminants**

I. INTRODUCTION

The marine environment plays an important role in maintaining ecological systems and biodiversity. However, due to human activities, such as chemical processes, industrial development, and urban expansion, contaminants can be introduced into the ocean, disrupting the ecosystem and biodiversity, and possibly leading to significant harmful effects on human health [1]. Contaminants in marine environments are transported through several mechanisms, including water flow-driven currents, sediment accumulation, and biological transfer through marine organisms. Among these, water flow-driven dispersion plays a major role. Researchers have been striving to model and characterize contaminants dispersion patterns [2], in order to further evaluate their impacts on the environment.

Dispersion reflects the spatial and temporal spread of contaminants in the ocean. Previous studies have investigated various approaches to simulate the dispersion process, including first-principles-based and data-driven approaches. First-principles-based methods, such as the finite-element method (FEM) [3] and finite-difference method (FDM) [4], provide a general framework for solving partial differential equations (PDEs), which is the fundamental mathematical description of the dispersion process. For example, Amrani et al. [5] utilized the multilevel adaptive semi-Lagrangian FEM to simulate pollution transport in the Mediterranean Sea. Liu et al. [6] applied the dynamic transient FEM to discretize PDEs into a linear state space model, transforming the pollutant dispersion modeling problem into a state estimation problem. Similarly, Li et al. [7] established a compact finite-difference scheme of a 2D time-fractional convection-diffusion equation for groundwater pollution transport problems. On the other hand, data-driven methods, such as neural networks (NNs), model dispersion processes by utilizing observational data. Instead of solving PDEs directly, these methods approximate dispersion dynamics through NNs, provided this is with sufficient training data. For example, He et al. [8] developed a physics-informed NNs-based, discretization-free method for solving coupled advection-dispersion and Darcy flow equations. Bertels et al. [9] proposed a physics-informed NN-based model for predicting the salinization of navigable waterways in Belgium.

Although these existing models can, to some extent, capture the evolution of contaminant dispersion, several limitations remain to be addressed. Data-driven methods rely on large amounts of high-quality observation data [10] and often lack physical interpretability, which is essential for engineering practice. For the FEM, the computation time and computer memory requirements are, in general, high [11]. In addition, when the convection dominates in the dispersion process, convergence becomes an essential concern [12]. Although the FDM is straightforward to implement, it still introduces numerical instability and oscillations in certain cases [13]. Moreover, the Courant–Friedrichs–Lewy (CFL) condition limits the time step size according to the spatial resolution, increasing the computational cost [14].

To address these problems, we extend the cell-based model (CBM), initially designed in the context of airborne traffic

Funded by the European Union under grant agreement 101134929 (ONE-BLUE). Views and opinions expressed are however those of the authors only and do not necessarily reflect those of the European Union or European Research Executive Agency. Neither the European Union nor the granting authority can be held responsible for them.

emission simulation [15], to simulate the dispersion process of contaminants in the marine environment. The emission model of [15] divides the 2D spatial domain into cells of equal dimensions and calculates pollution levels for each cell. Basically, for the evolution of emission levels within each cell, the influence of emissions from its neighboring cells is considered as well as the impact of external factors such as industrial or other local pollution. In general, the model considers two effects: convection and diffusion. To capture diffusion characteristics, the researchers define an expansion factor of the emissions in each cell. Moreover, when there is wind, the expanded emission cell is displaced along the wind direction [15].

Similarly, in the context of contaminant dispersion in the marine environment, we also focus on the same scenarios: convection and diffusion. Moreover, convection is driven by the water flows, which may vary in time and — in contrast to [15] — also in space, and diffusion is determined by the diffusion coefficient. Additionally, we propose two approaches to estimate the diffusion coefficient, and compare the results with those calculated from the first-order upwind scheme FDM, identifying the most accurate approach. Furthermore, we compare the CBM results with the FEM and the FDM, showing that the CBM is less sensitive to the CFL conditions compared to the FDM and provides a favorable trade-off between computational efficiency and accuracy under coarse resolutions.

This paper is organized as follows. In Section II, the enhanced CBM for contaminant dispersion in the marine environment is established. In Section III, two approaches for fitting the diffusion coefficient are proposed, and their accuracy is discussed. In Section IV, a comparative case study among the CBM, the FEM, and the FDM is conducted. Section V is the conclusions and discussion of future work.

II. CELL-BASED MODEL STRUCTURE

A. Convection process

Considering the marine environment as a two-dimensional plane, we divide this area into cells with the cell side length L. In addition, we discretize the time domain with T as the length of the time step.

The water flow can vary both in time and space. We define the positive x-axis direction as the reference direction, corresponding to the flow angle of 0 degrees. Angles in the counterclockwise direction are considered positive. Therefore, the flow direction can be described by the angle $\theta_{\text{flow}} \in [0, 2\pi)$. To simplify the calculation, we define the acute angle between the flow direction θ_{flow} and the x-axis as θ. This is illustrated in Fig. 1, where the flow direction is divided into four cases based on its position relative to the coordinate system. For each case, the angle θ can be expressed as

$$\theta = \begin{cases} \theta_{\text{flow}} & \text{if } \theta_{\text{flow}} \in [0, \frac{\pi}{2}) \\ \pi - \theta_{\text{flow}} & \text{if } \theta_{\text{flow}} \in [\frac{\pi}{2}, \pi) \\ \theta_{\text{flow}} - \pi & \text{if } \theta_{\text{flow}} \in [\pi, \frac{3\pi}{2}) \\ 2\pi - \theta_{\text{flow}} & \text{if } \theta_{\text{flow}} \in [\frac{3\pi}{2}, 2\pi) \end{cases} \tag{1}$$

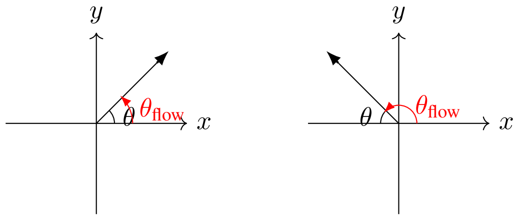

(a) Right-up flow (b) Left-up flow

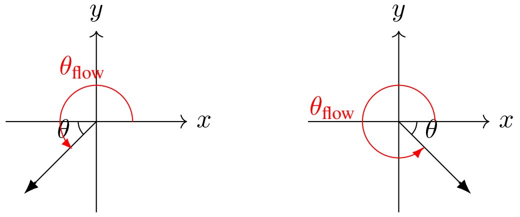

(c) Left-down flow (d) Right-down flow

Fig. 1: Flow direction in different quadrants

Let us suppose that the concentration of the contaminants at time step k in cell $C_{i,j}$ is $J_{i,j}(k)$. Then during the time period $[kT, (k+1)T)$, under the influence of the water flow velocity, the concentration of contaminants in the cell $C_{i,j}$ is affected by the neighboring cells. The contaminants from the neighbors on the upstream side will flow into the current cell, while the contaminants from the current cell will flow into the neighbors on the downstream side, which yields

$$\begin{aligned} J_{i,j}(k+1) = {} & J_{i,j}(k) \\ & + \sum_{(u,v)\in N_{\text{upstream}}(i,j,\theta_{\text{flow}})} \frac{\alpha_{u,v}^{i,j}(k)}{L^2(k)} J_{u,v}(k) \\ & - \sum_{(u,v)\in N_{\text{downstream}}(i,j,\theta_{\text{flow}})} \frac{\alpha_{u,v}^{i,j}(k)}{L^2(k)} J_{i,j}(k) \end{aligned} \tag{2}$$

where $\alpha_{u,v}^{i,j}(k)$ denotes the intersection area between the cell $C_{i,j}$ and its neighbor cell $C_{u,v}$ at time step k. Additionally, N_{upstream} and $N_{\text{downstream}}$ indicate the upstream and downstream neighbors, respectively.

As shown in Fig. 2, for example, let us assume a left-up flow velocity direction. The concentration movement of the current cell $C_{i,j}$ is due to the water flow velocity $V_{\text{f},i,j}(k)$ with a direction $\theta_{i,j}(k)$. To ensure numerical stability, the CFL condition requires that $\max(|TV_{\text{f},i,j}(k)\cos\theta_{i,j}(k)|, |TV_{\text{f},i,j}(k)\sin\theta_{i,j}(k)| \leq L$ [16], which means that in one time step, particles should not be able to cross more than their closest neighboring cells. The relative center point $(0,0)$ of the current cell would move to (x_0, y_0). In this case, the contaminants in the current cell flow into its three downstream neighboring cells: the left neighbor, the upper neighbor, and the upper-left corner neighbor. In the meantime, the current cell receives contaminants from the upstream neighbors.

To calculate the interaction area $\alpha_{u,v}^{i,j}(k)$, we define the side lengths in the x-axis direction as a_1 and a_2, and in the y-axis direction as b_1 and b_2, as indicated in Fig. 2. These lengths are derived from the displacement vector $(x_0, y_0) = (TV_{\mathrm{f},i,j}(k)\cos\theta_{i,j}(k), TV_{\mathrm{f},i,j}(k)\sin\theta_{i,j}(k))$ based on triangular geometry, given as

$$\begin{aligned} a_1 &= TV_{\mathrm{f},i,j}(k)\cos\theta_{i,j}(k) \\ a_2 &= L - a_1 \\ b_1 &= TV_{\mathrm{f},i,j}(k)\sin\theta_{i,j}(k) \\ b_2 &= L - b_1 \end{aligned} \tag{3}$$

The interaction area $\alpha^{i,j}_{u,v}(k)$ is calculated as the product of these lengths for specific regions. Specifically, in Fig. 2, a_1b_1 represents the intersection area for the left-up corner cell, where the index is $(u = i-1, v = j-1)$; a_1b_2 represents the interaction area for the left cell, where the index is $(u = i-1, v = j)$; a_2b_1 represents the interaction area for the up cell, where the index is $(u = i, v = j-1)$.

These interacting regions correspond to the overlapping areas determined by the displacement vector. While the example in Fig. 2 assumes the water flow direction is towards the left-up area, this derivation of a_1, a_2, b_1, b_2 is general. In other words, (3) applies to any water flow direction, as θ is defined as the acute angle between the water flow direction θ_{flow} and the x-axis. It relies on the geometric projection of the displacement vector and is independent of the specific flow direction.

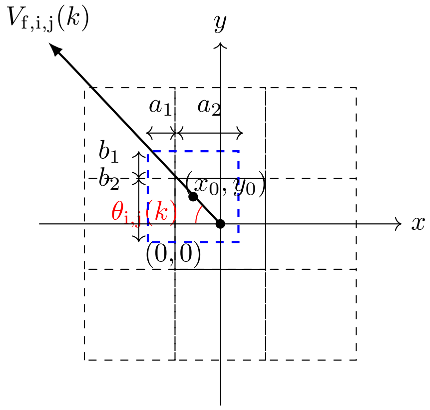

Fig. 2: The movement of contaminants from the current cell towards downstream cells under the influence of water flow velocity.

B. Diffusion process

In the diffusion process, according to the entropy increase principle, the contaminants move from the area of high concentration to the area of low concentration. Intuitively, this process could be considered as the expansion of concentration.

During the time period $[kT, (k+1)T)$, under the influence of the concentration expansion, the concentration of contaminants in the cell $C_{i,j}$ is also affected by its neighbors. The following will explain this process in detail, as shown in Fig. 3.

For the outflow of the current cell, assume that the current concentration of the neighboring cells is 0. Consequently, the contaminants of the current cell spread to the neighboring cells, and the driver is the current cell concentration, which leads to

$$J_{i,j}(k+1) = J_{i,j}(k) - \sum_{(u,v)\in N(i,j)} J_{i,j}(k)\frac{\beta^{i,j}_{u,v}(k)}{L_{\mathrm{d}}^2} \tag{4}$$

where $\beta^{i,j}_{u,v}(k)$ denotes the intersection area between cell $C_{i,j}$ and its neighbor cell $C_{u,v}$ at time step k. Moreover, L_{d} is the side length of the cells after diffusion, given by $L_{\mathrm{d}} = (1+T\lambda_{\mathrm{c}})L$, where λ_{c} is the diffusion coefficient in the CBM. Additionally, $N(i,j)$ indicates the neighboring cells.

Similarly, for the inflow of the current cell, assuming that the current cell concentration is 0, the contaminants of the neighboring cells all flow into the current cell, and the driver is the concentration of the surrounding cells, which leads to

$$J_{i,j}(k+1) = J_{i,j}(k) + \sum_{(u,v)\in N(i,j)} J_{u,v}(k)\frac{\beta^{i,j}_{u,v}(k)}{L_{\mathrm{d}}^2} \tag{5}$$

Since the diffusion process is linear, the superposition principle can be applied. Therefore the effects of the two diffusion processes can be added together, which yields

$$\begin{aligned} J_{i,j}(k+1) &= J_{i,j}(k) \\ &+ \sum_{(u,v)\in N(i,j)} (J_{u,v}(k) - J_{i,j}(k))\frac{\beta^{i,j}_{u,v}(k)}{L_{\mathrm{d}}^2} \end{aligned} \tag{6}$$

The term $J_{u,v}(k) - J_{i,j}(k)$ represents the concentration difference between the neighbor cell $C_{u,v}$ and the current cell $C_{i,j}$, and this difference is known as the concentration gradient.

As shown in Fig. 3, for example, let us consider the contaminants of the cell $C_{i,j}$ expanding into its closest neighbor cells. In this case, the cell $C_{i,j}$ interacts with four corner cells and four horizontal and vertical cells. To determine $\beta^{i,j}_{u,v}$, we define the side lengths of interaction areas as e_1 and e_2, respectively. Here, e_1 is derived from the diffusion coefficient of the CBM, while e_2 is equal to L, given as

$$\begin{aligned} e_1 &= TL\lambda_{\mathrm{c}} \\ e_2 &= L \end{aligned} \tag{7}$$

The interaction area $\beta^{i,j}_{u,v}$ is calculated as the product of these lengths for specific regions. More specifically, in Fig. 3, e_1e_1 represents the interaction area for the four corner cells, where the indices are $(u = i-1, v = j-1)$, $(u = i+1, v = j+1)$, $(u = i-1, v = j+1)$, and $(u = i+1, v = j-1)$. Additionally, e_1L represents the interaction area for the horizontal and vertical cells, where the indices of horizontal cells are $(u = i+1, v = j)$ and $(u = i-1, v = j)$, while the indices of vertical cells are $(u = i, v = j+1)$ and $(u = i, v = j-1)$.

III. Fitting the diffusion coefficient

In the previous section, we introduced the CBM structure, which includes the convection and diffusion components. In the diffusion component, we defined λ_{c} as the diffusion coefficient. However, for the fundamental convection-diffusion PDE, the diffusion component is given as $\lambda_{\mathrm{f}}\nabla^2 J$ [6], where

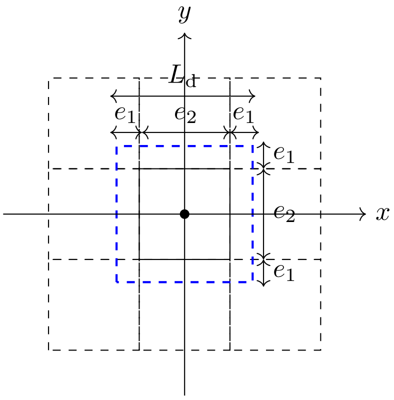

Fig. 3: The current cell expansion under the influence of concentration of contaminants.

λ_f is the diffusion coefficient and ∇^2 represents the Laplacian operator. In other words, this λ_f is not physically equivalent to λ_c. In order to make λ_c more physically interpretable, we propose two approaches to link λ_f and λ_c, and then to fit them accordingly.

A. Approach 1: relation under equal grid configurations

The diffusion component of the convection-diffusion PDE can be discretized using the FDM with a central difference scheme [17], given as

$$\begin{aligned} J_{i,j}(k+1) = J_{i,j}(k) + \lambda_\mathrm{f}\left(\frac{T}{L^2}\right)(J_{i-1,j}(k) \\ + J_{i+1,j}(k) + J_{i,j-1}(k) \\ + J_{i,j+1}(k) - 4J_{i,j}(k)) \end{aligned} \tag{8}$$

The diffusion component of the CBM, as we discussed in the previous section, is computed by considering the expanding area ratio. The coefficient of the formulas is given as

$$\frac{\beta^{i,j}_{u,v}(k)}{L_\mathrm{d}^2} = \begin{cases} \frac{T\lambda_\mathrm{c}}{(1+T\lambda_\mathrm{c})^2}, & \text{for the four horizontal and vertical neighbors} \\ \left(\frac{T\lambda_\mathrm{c}}{1+T\lambda_\mathrm{c}}\right)^2, & \text{for the four corner neighbors} \end{cases} \tag{9}$$

Equaling the coefficients of four horizontal and vertical cells in (8) with those of (6) and taking (9) into account, we get

$$T^2\lambda_\mathrm{c}^2 + \left(2T - \frac{L^2}{\lambda_\mathrm{f}}\right)\lambda_\mathrm{c} + 1 = 0 \tag{10}$$

By solving this quadratic equation, we can obtain the relationship between λ_c and λ_f. Specifically, by applying the quadratic formula and making some simplifications, we get the roots, which yields

$$\lambda_\mathrm{c} = \frac{L}{2\lambda_\mathrm{f}T^2}(L \pm \sqrt{L^2 - 4T\lambda_\mathrm{f}}) - \frac{1}{T} \tag{11}$$

The appropriate physically meaningful root is selected depending on the value of λ_f. When λ_f is small, the minus sign has to be chosen, whereas when λ_f is large, the plus sign has to be used.

B. Approach 2: identification based on simulation data

Alternatively, to determine the optimal coefficient λ_c in the CBM, a nonlinear least-squares optimization approach can be used based on data generated from an FDM model with the same initial conditions and the same water flow profiles. The optimization problem can be formulated as:

$$\min_{\lambda_\mathrm{c}} \sum_{k=1}^{N} \sum_{(i,j)\in G} (J_{\mathrm{FDM},i,j}(k) - J_{\mathrm{CBM},i,j}(k,\lambda_\mathrm{c})) \tag{12}$$

where G represents the collection of grid cells. $J_{\mathrm{FDM},i,j}(k)$ represents the output values of the FDM at spatial index (i,j) and time step k, and $J_{\mathrm{CBM},i,j}(k,\lambda_\mathrm{c})$ represents the output values of the CBM at spatial index (i,j) and time step k, with parameter λ_c.

C. Case study

In order to validate the accuracy of the proposed approaches for linking λ_f and λ_c, numerical experiments are conducted on an $8\ \mathrm{m} \times 8\ \mathrm{m}$ physical domain, with background concentration initial value $1\ \mu\mathrm{g/m}^3$. The contaminants follow a Gaussian distribution in the middle of $2\ \mathrm{m} \times 2\ \mathrm{m}$ area, with a peak value of $100\ \mu\mathrm{g/m}^3$. The water flow is along the diagonal direction of the domain, with a velocity magnitude of $V_\mathrm{f} = 0.25\ \mathrm{m/s}$.

A wide range of λ_f values are considered, ranging from $1.8400 \cdot 10^{-7}\,\mathrm{m^2/s}$ to $0.01\,\mathrm{m^2/s}$. The CBM is defined with spatial step size $L_\mathrm{c} = 0.02$ m and time step size $T_\mathrm{c} = 2 \cdot 10^{-3}$ s. Each simulation runs for 5000 time steps, reaching a total simulation time of 10 s. To provide a more accurate reference solution, the corresponding FDM is computed on a finer grid configuration with $L_\mathrm{f} = 0.01$ m and $T_\mathrm{f} = 10^{-3}$ s to reduce numerical errors, and then mapped to the CBM grid size through spatial averaging.

Table I presents the RMSE values comparing each approach with the corresponding FDM solution. The results demonstrate that the identification approach (Section III-B) generally yields the lowest RMSE, indicating the higher accuracy between these two approaches. In addition, Approach 1 (Section III-A) offers a simpler and more straightforward formulation, making it favorable in scenarios where simple implementation is prioritized over accuracy.

IV. PERFORMANCE EVALUATION OF CBM, FDM, AND FEM

We conduct numerical experiments to validate the performance of the CBM with respect to a first-order upwind FDM [17] and a stabilized FEM solver [3]. The CBM and the FDM are implemented in Python, while the FEM is implemented using Python-COMSOL. The physical domain is defined as a $100\ \mathrm{m} \times 100\ \mathrm{m}$ area, with an initial background concentration value of $1.1\ \mu\mathrm{g/m}^3$. The contaminants follow a Gaussian distribution in a $60\ \mathrm{m} \times 60\ \mathrm{m}$ region in the lower left, with a peak value of $10\ \mu\mathrm{g/m}^3$, as shown in Fig. 4. The parameters are set as follows: the water flow has a velocity of magnitude $V_\mathrm{f} = 0.7\ \mathrm{m/s}$ at the angle of $\theta = \pi/4$. The diffusion coefficient is $\lambda_\mathrm{f} = 1.12 \times 10^{-3}\ \mathrm{m^2/s}$.

$\lambda_{\mathrm{f}}(\mathrm{m}^2/\mathrm{s})$	Method	$\lambda_{\mathrm{c}}(1/\mathrm{s})$	RMSE
$1.8400 \cdot 10^{-7}$	Approach 1	$4.6000 \cdot 10^{-4}$	$2.6535 \cdot 10^{-2}$
	Approach 2	$\mathbf{9.1545 \cdot 10^{-4}}$	$2.7699 \cdot 10^{-4}$
$7.4300 \cdot 10^{-7}$	Approach 1	$1.8575 \cdot 10^{-3}$	$9.7906 \cdot 10^{-2}$
	Approach 2	$\mathbf{3.6428 \cdot 10^{-3}}$	$3.6078 \cdot 10^{-3}$
$1.7200 \cdot 10^{-6}$	Approach 1	$4.3001 \cdot 10^{-3}$	$1.9430 \cdot 10^{-1}$
	Approach 2	$\mathbf{8.2077 \cdot 10^{-3}}$	$1.5725 \cdot 10^{-2}$
$6.9600 \cdot 10^{-6}$	Approach 1	$1.7401 \cdot 10^{-2}$	$3.6925 \cdot 10^{-1}$
	Approach 2	$\mathbf{2.8431 \cdot 10^{-2}}$	$9.4445 \cdot 10^{-2}$
$1.6100 \cdot 10^{-5}$	Approach 1	$4.0256 \cdot 10^{-2}$	$2.8838 \cdot 10^{-1}$
	Approach 2	$\mathbf{5.3735 \cdot 10^{-2}}$	$1.1037 \cdot 10^{-1}$
$6.5200 \cdot 10^{-5}$	Approach 1	$1.6311 \cdot 10^{-1}$	$8.0989 \cdot 10^{-2}$
	Approach 2	$\mathbf{1.7448 \cdot 10^{-1}}$	$3.0719 \cdot 10^{-2}$
$1.5100 \cdot 10^{-4}$	Approach 1	$3.7807 \cdot 10^{-1}$	$4.0406 \cdot 10^{-2}$
	Approach 2	$\mathbf{3.8861 \cdot 10^{-1}}$	$1.6965 \cdot 10^{-2}$
$6.1000 \cdot 10^{-4}$	Approach 1	$1.5344 \cdot 10^{0}$	$8.9051 \cdot 10^{-3}$
	Approach 2	$\mathbf{1.5358 \cdot 10^{0}}$	$8.7286 \cdot 10^{-3}$
$1.0000 \cdot 10^{-3}$	Approach 1	$2.7040 \cdot 10^{0}$	$1.6405 \cdot 10^{-2}$
	Approach 2	$\mathbf{2.6857 \cdot 10^{0}}$	$7.1860 \cdot 10^{-3}$
$4.3200 \cdot 10^{-3}$	Approach 1	$1.1293 \cdot 10^{1}$	$1.3974 \cdot 10^{-1}$
	Approach 2	$\mathbf{1.0815 \cdot 10^{1}}$	$4.7754 \cdot 10^{-3}$
$1.0000 \cdot 10^{-2}$	Approach 1	$2.7864 \cdot 10^{1}$	$4.5272 \cdot 10^{-1}$
	Approach 2	$\mathbf{2.5066 \cdot 10^{1}}$	$3.7908 \cdot 10^{-3}$

TABLE I: Fitted λ_{c} values and absolute RMSE for different approaches and λ_{f} values. *Note: The bold font indicates the λ_{c} value that yields the lowest RMSE between the two approaches.*

To evaluate the numerical performance of the CBM, the FDM, and the FEM, we design a set of numerical simulation experiments under different spatial and temporal resolutions. A total of 88 experiments are conducted, with the time step T varying from $0.01\,\mathrm{s}$ to $2.5\,\mathrm{s}$, and the spatial resolution L ranges from $0.1\,\mathrm{m}$ to $5\,\mathrm{m}$. Each simulation runs for 60 seconds, with the solution recorded every 10 seconds. The baseline FEM setting is $T = 0.01\,\mathrm{s}$ and $L = 0.1\,\mathrm{m}$.

For accuracy evaluation, we compute the relative Root Mean Square Error (RMSE) compared to the baseline, as shown in Fig. 5, which provides a comprehensive comparison of accuracy trends. The relative RMSE is calculated by

$$\text{Relative RMSE} = \sqrt{\frac{1}{|G|} \sum_{(i,j)\in G} \frac{\left(J_{\text{baseline},i,j} - J_{i,j}\right)^2}{J^2_{\text{baseline},i,j} + \epsilon}} \tag{13}$$

where $J_{\text{baseline},i,j}$ and $J_{i,j}$ represent baseline concentration values and current computed concentration values at each grid point (i, j), respectively. Furthermore, ϵ is a small positive value (10^{-10}), to avoid division by zero when the baseline values are close to zero. Additionally, the relative RMSE is computed at 10, 20, 30, 40, 50, and 60 seconds, based on snapshots saved every 10 seconds.

Moreover, to assess computational efficiency, the corresponding solver running time is recorded and analyzed, as presented in Fig. 6. The scripts all run in DelftBlue service, a computing service provided by Delft University of Technology, with each job utilizing 16 CPU cores of Intel(R) Xeon(R) Gold 6226R @ 2.90GHz and 32 GB memory.

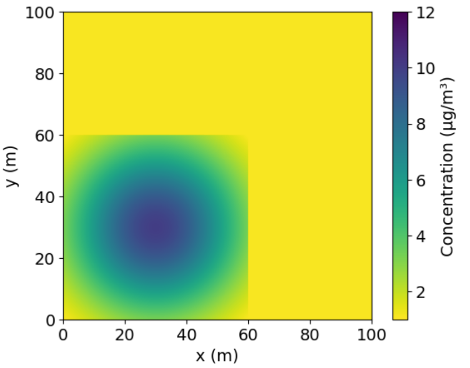

Fig. 4: Initial condition at simulation time $t = 0\,$seconds

A. *Performance evaluation near critical point*

Based on the relative RMSE trend in Fig. 5, we find that the CBM shows better convergence behavior than that of the FDM near the critical CFL condition point. For example, at $T = 2.0$ s, the CBM successfully converges under $L = 1\,\mathrm{m}$, with a relative RMSE of 3.0164%, and the computation time is 0.0078 seconds. In contrast, the FDM does not converge under the same conditions. The FDM requires a coarser grid (L $= 2\,\mathrm{m}$) to achieve convergence at the same time step $T = 2.0\,\mathrm{s}$, resulting in the RMSE being as high as 20.9448%. Alternatively, when $L = 1\,\mathrm{m}$ and T is reduced to 1 s, the FDM starts to converge but the RMSE reaches 15.1762% and the computation time is comparable to that of CBM, though slightly longer, reaching 0.0081 seconds.

Overall, the CBM is less affected by the CFL conditions than the FDM. On the one hand, under a fixed time step, the CBM converges reliably as the spatial resolution becomes finer, whereas the FDM either may fail to converge or produce higher errors. On the other hand, under a fixed spatial resolution, the CBM maintains stable convergence with larger time steps, while the FDM requires smaller time steps yet still produces higher errors with slightly more computation time.

B. *Performance evaluation in stable regimes*

From Fig. 5, we observe that the CBM and the FDM yield similar relative RMSE values when T ranges from $0.01\,\mathrm{s}$ to $1.25\,\mathrm{s}$ in the stable regimes, while the CBM produces smaller relative RMSE between $2.0\,\mathrm{s}$ and $5.0\,\mathrm{s}$. This indicates that as T increases, the difference in solution accuracy between the CBM and FDM becomes more noticeable, with the CBM being slightly more accurate than the FDM. Moreover, although the FEM consistently yields lower relative RMSE values, Fig. 6 shows that its running time is much higher than that of both the CBM and the FDM.

We now select four representative parameter combinations for detailed analysis, as shown in Table II and Table III, which present the accuracy and computation efficiency under different spatial and temporal settings. In these tables, sim. time denotes the simulation time, abs. diff represents the absolute difference $\mathrm{FDM} - \mathrm{CBM}$, and rel. diff indicates the relative difference $|\mathrm{FDM} - \mathrm{CBM}|/\mathrm{CBM}$.

From Table II, we observe that for larger time steps ($T = 2.0\,\mathrm{s}$), the CBM yields a smaller relative RMSE than the FDM, and the absolute difference between them increases over time. At simulation time $t = 60\,\mathrm{seconds}$, when $L = 2\,\mathrm{m}$, the absolute difference reaches 1.0215%, with a relative difference of 5.13%. When $L = 2.5\,\mathrm{m}$, the absolute and relative differences are 0.6778% and 2.81%, respectively. For smaller time steps ($T = 0.2\,\mathrm{s}$), both methods show nearly identical performance, with the FDM slightly more accurate than the CBM, and the maximum relative difference is only 0.07%. In addition, Table III shows that normally the FDM is approximately 45% faster than the CBM.

Overall, the CBM and the FDM demonstrate comparable accuracy in stable regimes, with the CBM performing slightly better at larger time steps and over longer simulation times. The FDM is approximately 45% faster than CBM, and both are significantly faster than the FEM.

Sim. time (s)	Method	$T = 2.0\text{s}$ $L = 2.0\text{m}$	$T = 2.0\text{s}$ $L = 2.5\text{m}$	$T = 0.2\text{s}$ $L = 2.0\text{m}$	$T = 0.2\text{s}$ $L = 2.5\text{m}$
10	FEM	3.5829	7.2303	3.8433	7.3265
	FDM	6.8894	11.6580	10.1951	14.2158
	CBM	6.7084	11.5683	10.2013	14.2203
	Abs. diff	0.1810	0.0897	-0.0062	-0.0045
	Rel. diff	0.0270	0.0078	0.0006	0.0003
20	FEM	7.5712	8.5616	7.8153	8.7405
	FDM	12.8841	15.3184	16.8476	18.7277
	CBM	12.5941	15.1126	16.8578	18.7359
	Abs. diff	0.2900	0.2058	-0.0102	-0.0082
	Rel. diff	0.0230	0.0136	0.0006	0.0004
30	FEM	7.2044	9.6034	7.3578	9.7042
	FDM	13.9302	18.1880	18.8172	22.3003
	CBM	13.4188	17.8606	18.8316	22.3115
	Abs. diff	0.5114	0.3274	-0.0144	-0.0112
	Rel. diff	0.0381	0.0183	0.0008	0.0005
40	FEM	9.1979	10.4474	9.2098	10.4519
	FDM	17.3480	20.6571	22.7176	25.3594
	CBM	16.6932	20.2084	22.7338	25.3728
	Abs. diff	0.6548	0.4487	-0.0162	-0.0134
	Rel. diff	0.0392	0.0222	0.0007	0.0005
50	FEM	9.3815	11.2429	9.2579	11.0956
	FDM	18.5375	22.8616	24.5356	28.0584
	CBM	17.6706	22.2962	24.5552	28.0738
	Abs. diff	0.8669	0.5654	-0.0196	-0.0154
	Rel. diff	0.0491	0.0254	0.0008	0.0005
60	FEM	10.4441	11.8745	10.3041	11.7009
	FDM	20.9448	24.8362	27.2239	30.2831
	CBM	19.9233	24.1584	27.2440	30.2998
	Abs. diff	1.0215	0.6778	-0.0201	-0.0167
	Rel. diff	0.0513	0.0281	0.0007	0.0006

TABLE II: Relative RMSE values (in percentage), the absolute and relative differences between the FDM and the CBM under different spatial and temporal resolutions.

Sim. time (s)	Method	$T = 2.0\text{s}$ $L = 2.0\text{m}$	$T = 2.0\text{s}$ $L = 2.5\text{m}$	$T = 0.2\text{s}$ $L = 2.0\text{m}$	$T = 0.2\text{s}$ $L = 2.5\text{m}$
60s	FEM	5.8028	4.8614	429.8666	339.4601
	FDM	0.0024	0.0020	0.1387	0.1195
	CBM	0.0044	0.0036	0.1388	0.1195
	Abs. diff	-0.0020	-0.0016	-0.0001	0.0000
	Rel. diff	0.4545	0.4444	0.0007	0.0000

TABLE III: Computation time (in seconds) at simulation time $t = 60\,\mathrm{seconds}$, and the absolute and relative differences between the FDM and the CBM under different spatial and temporal resolutions. *Note: Values are reported up to four decimals, and small differences may be caused by rounding.*

V. CONCLUSIONS AND FUTURE WORK

We have proposed an enhanced cell-based model (CBM) for simulating contaminant dispersion in marine environments. Through derivation and performance evaluation, we draw the following conclusions:

1) The enhanced CBM is suitable for large-scale simulations due to its naturally parallelizable structure. Moreover, it can handle time — and space — varying flow fields and allow physical interpretability through coefficient identification, making it practical for marine contaminant dispersion applications.
2) The experimental results show that the CBM is less affected by the Courant–Friedrichs–Lewy (CFL) conditions compared to the finite-difference method (FDM). This stability allows the CBM to maintain convergence where the FDM may fail or requires a coarser spatial discretization and a smaller time step to achieve convergence, providing a potential solution for improved computational efficiency without sacrificing solution accuracy near the CFL boundary.
3) The CBM offers a favorable trade-off between accuracy and efficiency under coarse resolutions, even though the accuracy may remain limited in such regimes.

For the next stage of our work, we will follow the overall goal of monitoring and assessing contaminants in ocean environments, focusing on exploring two main directions:

1) Extension of the CBM framework: We plan to extend the current CBM to three-dimensional domains and incorporate chemical reactions into the transport process, providing a more comprehensive and realistic framework for contaminant dispersion.
2) Modeling and prediction under sparse measurements: We aim to integrate numerical solvers — such as CBM, FDM, or FEM — with physics-informed neural networks, in order to achieve accurate and physically consistent spatiotemporal predictions of contaminant concentrations under sparse measurements.

REFERENCES

[1] K. Y.-H. Gin, C. Ng, W. Li, S. G. Goh, X. Tong, and M. C. Jong, "Emerging Microbial Contaminants in the Ocean," in *Oceans and Human Health*. Elsevier, 2023, pp. 315–350.

[2] S. B. Grant, J. H. Kim, B. H. Jones, S. A. Jenkins, J. Wasyl, and C. Cudaback, "Surf zone entrainment, along-shore transport, and human health implications of pollution from tidal outlets," *Journal of Geophysical Research: Oceans*, vol. 110, no. C10, 2005.

[3] M. G. Larson and F. Bengzon, *The Finite Element Method: Theory, Implementation, and Applications*. Springer Science & Business Media, 2013, vol. 10.

[4] J. W. Thomas, *Numerical Partial Differential Equations: Finite Difference Methods*. Springer Science & Business Media, 2013, vol. 22.

[5] M. El-Amrani, A. Ouardghi, and M. Seaid, "Modeling and Simulation of Pollution Transport in the Mediterranean Sea Using Enriched Finite Element Method," *Mathematics and Computers in Simulation*, vol. 223, pp. 565–587, 2024.

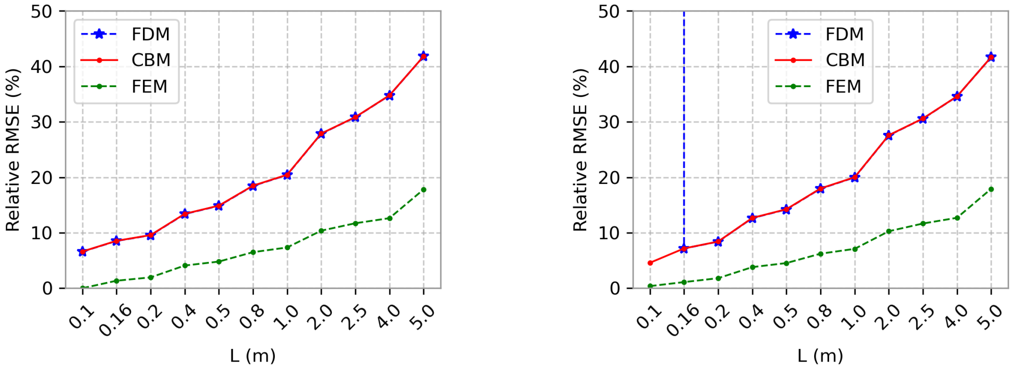

(a) Accuracy evaluation for T = 0.01 s

(b) Accuracy evaluation for T = 0.1 s

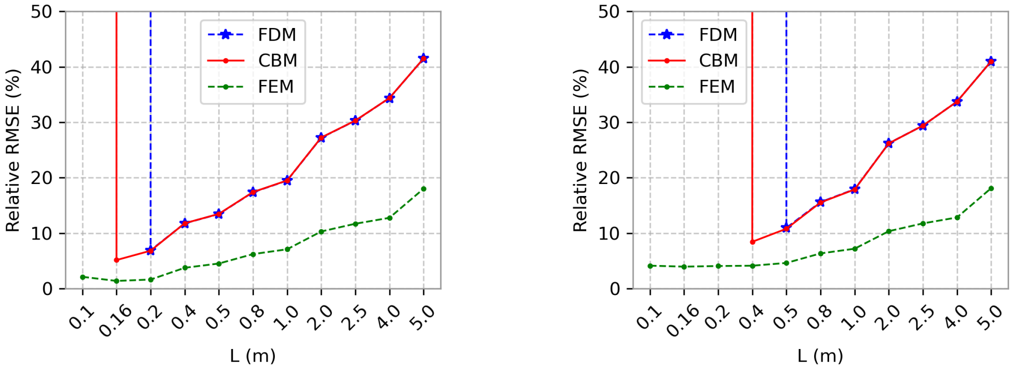

(c) Accuracy evaluation for T = 0.2 s

(d) Accuracy evaluation for T = 0.5 s

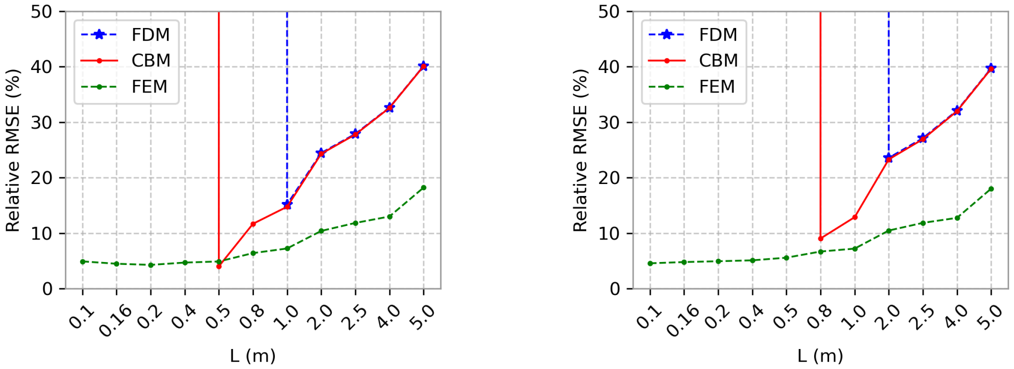

(e) Accuracy evaluation for T = 1.0 s

(f) Accuracy evaluation for T = 1.25 s

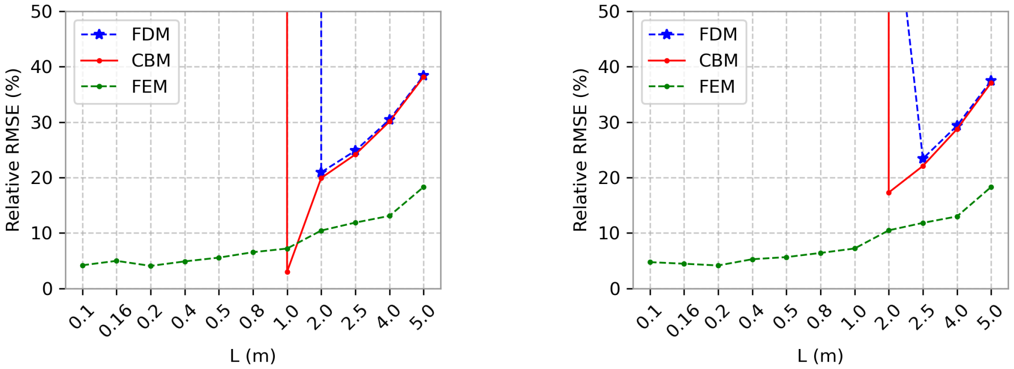

(g) Accuracy evaluation for T = 2.0 s

(h) Accuracy evaluation for T = 2.5 s

Fig. 5: Relative RMSE at simulation time $t = 60\,\text{seconds}$ (values in percentage)

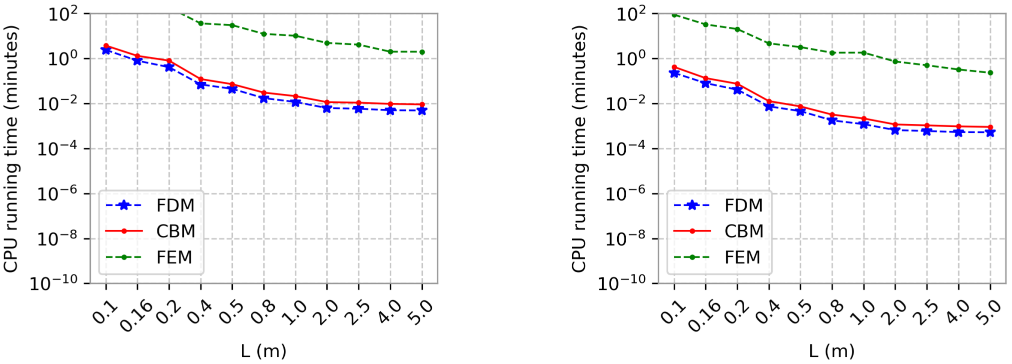

(a) Solving time for T = 0.01 s

(b) Solving time for T = 0.1 s

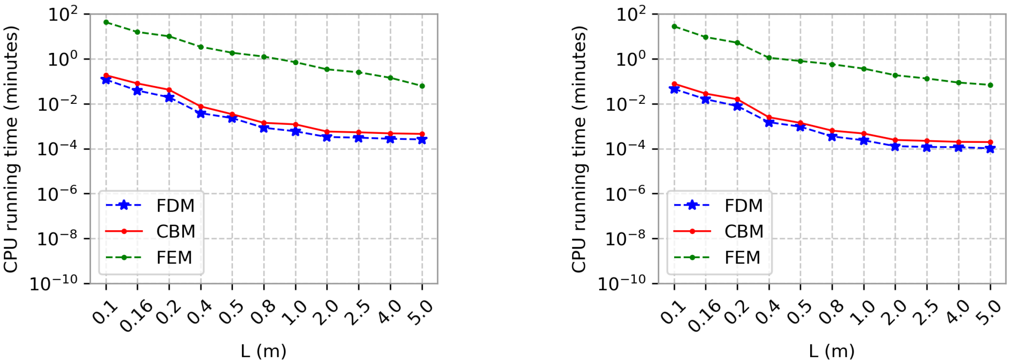

(c) Solving time for T = 0.2 s

(d) Solving time for T = 0.5 s

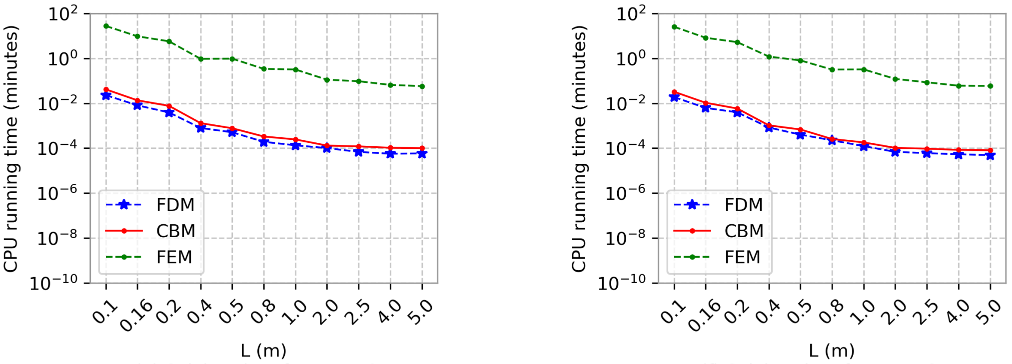

(e) Solving time for T = 1.0 s

(f) Solving time for T = 1.25 s

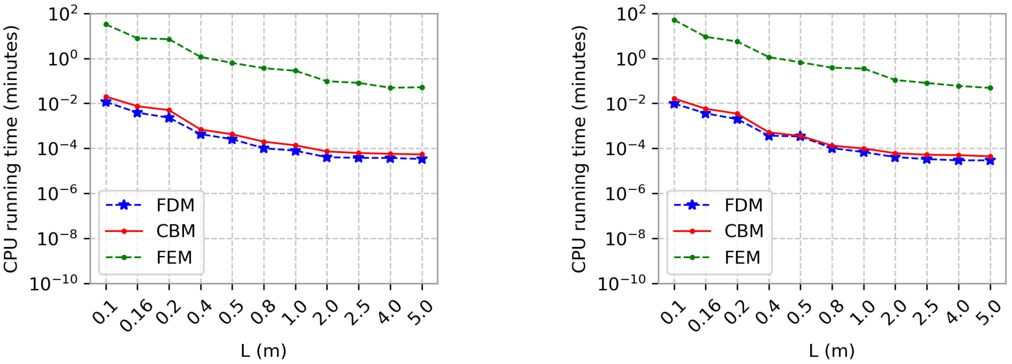

(g) Solving time for T = 2.0 s

(h) Solving time for T = 2.5 s

Fig. 6: Computation time at simulation time $t = 60\,\mathrm{seconds}$

[6] Y. Liu, C. M. Harvey, F. E. Hamlyn, and C. Liu, “Bayesian Estimation and Reconstruction of Marine Surface Contaminant Dispersion,” *Science of the Total Environment*, vol. 907, p. 167973, 2024.

[7] L. Li, Z. Jiang, and Z. Yin, “Compact Finite-Difference Method for 2D Time-Fractional Convection–Diffusion Equation of Groundwater Pollution Problems,” *Computational and Applied Mathematics*, vol. 39, no. 3, p. 142, 2020.

[8] Q. He and A. M. Tartakovsky, “Physics-Informed Neural Network Method for Forward and Backward Advection-Dispersion Equations,” *Water Resources Research*, vol. 57, no. 7, p. e2020WR029479, 2021.

[9] D. Bertels and P. Willems, “Physics-Informed Machine Learning Method for Modelling Transport of a Conservative Pollutant in Surface Water Systems,” *Journal of Hydrology*, vol. 619, p. 129354, 2023.

[10] J. Chi and H.-c. Kim, “Prediction of Arctic Sea Ice Concentration Using a Fully Data Driven Deep Neural Network,” *Remote Sensing*, vol. 9, no. 12, p. 1305, 2017.

[11] P. Paul and J. Webb, “Reducing Computational Costs Using a Multi-Region Finite Element Method for Electromagnetic Scattering,” *IET Microwaves, Antennas & Propagation*, vol. 2, no. 5, pp. 427–433, 2008.

[12] A. Sendur, “A Comparative Study on Stabilized Finite Element Methods for the Convection-Diffusion-Reaction Problems,” *Journal of Applied Mathematics*, vol. 2018, no. 1, p. 4259634, 2018.

[13] P.-W. Li and F. Zhang, “A Weighted–Upwind Generalized Finite Difference (WU–GFD) Scheme with High–Order Accuracy for Solving Convection–Dominated Problems,” *Applied Mathematics Letters*, vol. 150, p. 108970, 2024.

[14] C. Hirsch, *Numerical Computation of Internal and External Flows: the Fundamentals of Computational Fluid Dynamics*. Elsevier, 2007.

[15] S. K. Zegeye, B. De Schutter, J. Hellendoorn, and E. A. Breunesse, “Variable Speed Limits for Area-Wide Reduction of Emissions,” in *13th International IEEE Conference on Intelligent Transportation Systems*. IEEE, 2010, pp. 507–512.

[16] C. A. De Moura and C. S. Kubrusly, “The Courant-Friedrichs-Lewy (CFL) condition,” *AMC*, vol. 10, no. 12, pp. 45–90, 2013.

[17] R. J. LeVeque, *Finite Difference Methods for Ordinary and Partial Differential Equations: Steady-State and Time-Dependent Problems*. SIAM, 2007.